Flow of Foams

Katgert, G.

Citation

Katgert, G. (2008, December 11). *Flow of Foams*. *Casimir PhD Series*. Retrieved from https://hdl.handle.net/1887/13329

CHAPTER 3

RHEOLOGY OF TWO DIMENSIONAL FOAMS IN A TAYLOR-COUETTE GEOMETRY

To test and expand the applicability of the drag force balance model developed in the last chapter, we perform experiments on bidisperse monolayers of foam bubbles, sheared in a Taylor-Couette geometry. In contrast to the linear geometry used in the previous chapter, the Couette geometry allows to study the flow of bubble rafts, i.e., 2D foams not trapped under a top plate. Also, its curved geometry means that the yielding threshold included in the expression for $\overline{F}_{bb}$ should play a role. We record averaged velocity profiles both with and without a bounding glass plate.

Our main finding is that two-dimensional foam flows in a Couette geometry with a top plate exhibit rate dependent and strongly shearbanded flows, whereas bubble raft flows are much less shearbanded and rate independent. We can fit the flows without a top plate to both a power law fluid model and solutions to the drag force balance model provided the local stresses scale with the local strain rate $\dot{\gamma}$ as $\tau = k\dot{\gamma}^{0.21}$. This is corroborated by direct measurements of the local stress-strain rate relation. In contrast, our drag force model fits poorly to the flows with a top plate if $\beta = 0.21$, but we do not succeed in establishing an optimal value of β in that case.

Strikingly, the model fits adequately only if we assume that the yield drag force — of which we should see the effects in the Couette geometry, in contrast to the linear geometry — is 0 or at least one order of magnitude smaller than what was measured in the previous chapter from the bulk rheometry a two-dimensional foam. This suggests that foams in a Taylor-Couette geometry still flow if the local stress is considerably below the globally measured yield stress.

3.1 Introduction

The flow of two dimensional foams has mainly been studied in Taylor-Couette geometries. For example, Dennin and coworkers have sheared bubble rafts in a Couette geometry with a fixed inner disc and a rotating outer cylinder [8, 71]. Debrégeas has confined foam bubbles in a Hele-Shaw cell and rotated the inner disc, while keeping the outer cylinder fixed [9]. In both cases, shear banded flow profiles where found. However, there has been no clear consensus on the cause of the shear bands in these systems, but clearly both the radial decay of the shear stress in curved geometries and the presence of a top-plate need to be considered. Cheddadi et al. [81] claim the wall drag that results from the top plate is not the main cause of shear banding: instead they attribute the shear banding to the inhomogeneity of the stresses which decay as $1/r^2$, see Appendix 3.A for a derivation. Scheibert et al. [72] instead claim that focusing of the stresses due to the quadrupolar stress field resulting from a T1 lies at the root of the shear banding.

Our strategy for disentangling the roles of wall drag and curvature is to fit flow profiles, obtained for a range of driving rates in Couette geometries with and without a top plate, to the Herschel-Bulkley-like model which described the flow in the linear geometry of chapter 2 in detail. Note that the velocity profiles measured by Gilbreth, Sullivan and Dennin [68] were also with some success fit to solutions of a Herschel-Bulkley constitutive equation, which suggests that our previously developed model might be applicable in the cylindrical geometry as well. An additional hint in that direction is that the continuum model that was postulated by Janiaud et al. [10] to describe two-dimensional foam flows with an additional wall drag, can be applied to the cylindrical geometry [82] and at least qualitatively, Krishan and Dennin [83] have obtained experimental confirmation of a few of their predictions.

Apart from the role of wall drag and curvature, an additional important issue is whether the transition from the flowing region to the stationary region is continuous: most earlier literature finds a discontinuous transition between a flowing and a non-flowing part in complex fluids: for instance Dennin and coworkers claim in [71] that the transition is discontinuous. Such discontinuous shear bands are also often observed in polymer systems and have also recently been observed by MRI imaging of the rheology of three-dimensional foams and emulsions [84, 85]. For the curved geometry, a discontinuous transition between the flowing and stationary flow can be seen as a direct consequence of the existence of a finite yield threshold: a part of the system that experiences local stresses below the yield stress will not flow and a region that is above the yield stress will.

For linear geometries as discussed in Chapter 2, the yield stress drops out and no discontinuity is found — similarly Wang, Krishan and Dennin find continuous shear bands in linearly sheared foams [66, 86]. In the curved geometry the yield stress cannot be ignored and if there were an appreciable yield stress we would observe this in our fitting procedure. Moreover, one could expect to see a discontinuity in the experimental velocity profiles providing a clear signature of the presence of a yield stress.

We will measure velocity profiles of two-dimensional foams in a Taylor-Couette geometry. We can study two cases. First, we add a top glass plate to study shear localization in a setup that is very similar to the Hele-Shaw type cell employed by Debrégeas et al. [9]. Second, we will also study flows without top plate, to investigate possibly discontinuous shear banding in a bubble raft geometry akin to the one employed by Dennin and coworkers. Surprisingly, we will see that our system, in stead of resolving these issues, merely raises new ones. First, we find essentially continuous flow profiles and the corresponding fitted values of the yield stress are at least an order of magnitude smaller than what was obtained from rheometry. Second, our power law exponent for systems with and without top plate differ. Third, a close comparison of the local rheology with the global rheology finds puzzling discrepancies.

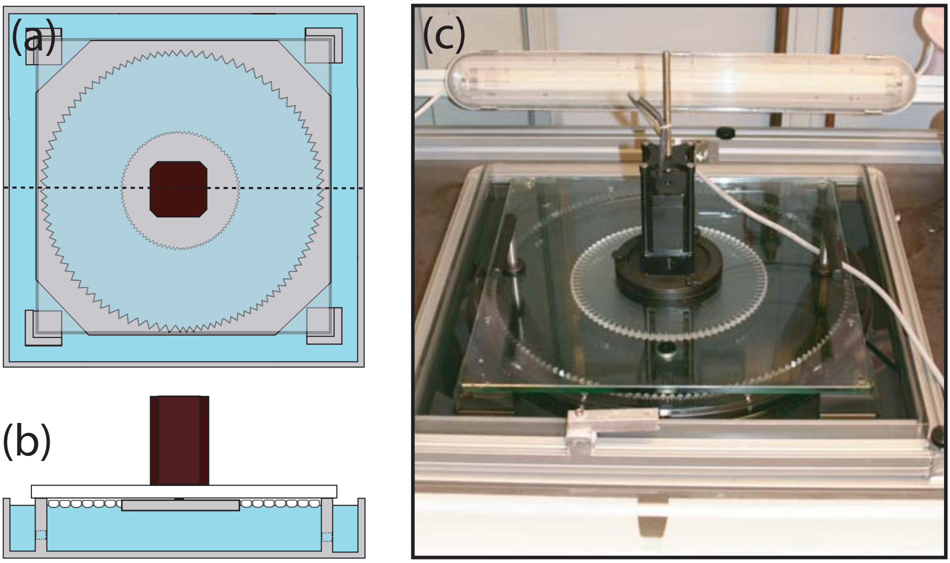

Figure 3.1: (a) Schematic top view of Taylor-Couette cell used in this experiment. The outer cylinder, reservoirs and supports for the glass plate have been milled into a PMMA block. (b) Side view: the reservoirs and the bounded area are connected to keep the region underneath the glass plate from draining. The motor is connected to the inner cylinder through the glass plate. (c) Photograph of the experimental setup.

3.2 Experiment

3.2.1 Setup

Our experimental setup consists of a 500 by 500 by 50 mm square PMMA block, into which the outer cylinder, a reservoir and supports for a removable glass plate are milled, see Fig. 3.1. The boundary of the reservoir acts as the outer cylinder (of radius $r_o = 190$ mm) and is grooved with 6 mm grooves. On the glass plate of 405 by 405 by 12 mm, two handles and a casing for a stepper motor are fixed by UV curing glue. The stepper motor (L-5709 Lin engineering) is connected to an inner cylinder of $r_i = 105$ mm radius through a hole in the glass plate. The inner cylinder is grooved like the outer cylinder. The region that is filled with bubbles is in direct contact with the reservoirs outside the glass plate. This is to keep the liquid level underneath the glass plate constant, as fluid that has left the shearing region due to capillary suction will reenter the system in the outside reservoirs.

A bidisperse foam is produced by filling the reservoir with the same soap solution as used previously and immersing syringe needles of two inner diameters, bubbling nitrogen through bothy needles and subsequently thoroughly mixing the resulting bubbles. The resulting bubble sizes are as before: $d_1, d_2 = 1.8,\ 2.7$ mm. The glass plate, with the inner driving wheel attached, is carefully placed on top of the foam and subsequently, the foam is allowed to equilibrate for a considerable time. Approximately 40 bubble layers are contained within the gap.

3.2.2 Imaging

The foam is lit laterally by 4 fluorescent tubes driven by HF ballasts and images are recorded by a CCD camera (Foculus FO 432BW), equipped with a Tamron 280-300 telezoomlens. The bottom of the reservoir is black, to enhance contrast. The frame rate is fixed such that the angular displacement of the inner cylinder is fixed at $1.12{\times}10^{-3}$ rad/frame. We record only during steady shear, ensuring that the foam has been sheared considerably before starting image acquisition.

We calculate velocity profiles across the gap between inner and outer wheel by cross correlating arcs of fixed radial distance in subsequent frames over a large angular region. While this improves statistics, it forces us to calculate velocity profiles on curved image lines. However, by defining circular arcs and identifying these with the appropriate pixels, this can easily be done, see Fig. 3.2. We compute averaged velocities over 2000 frames for the slowest runs with a top plate, 10000 frames for the fastest runs with a top plate and over 3000 frames for the bubble raft experiment, to enhance statistics. We check that coarsening, coalescence and rupturing are absent in the runs with a top plate, whereas we cannot rule out the latter two phenomena in the bubble raft experiment. There we merely content ourselves with the absence of holes in our foam during the experiment, which can be achieved by loading the Couette cell with a surplus of foam far away from the imaging region.

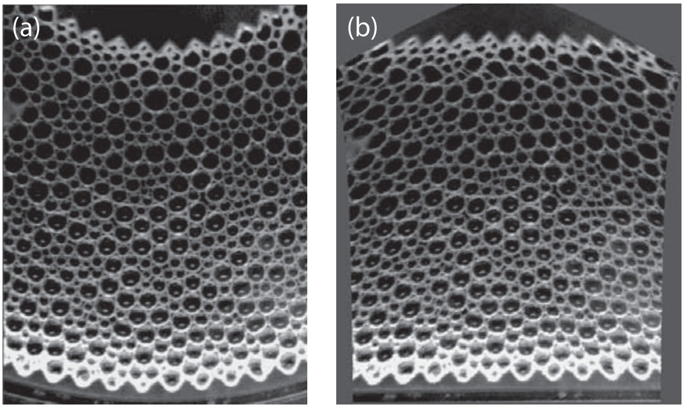

FIGURE 3.2: (a) Raw image as obtained by CCD camera. The local curvature is extracted from the curvature at the inner disc and the outer cylinder, and for every r we define an arc that we match to pixels in the image. If we plot these arcs as straight lines we obtain: (b) the image with correction for curvature. We compute cross correlations between subsequent frames on these straightened image lines.

3.3 Results

We shear the foam, covered with a glass plate at 6 different driving velocities, spanning 2.5 decades. Results are plotted in Fig. 3.3. We have rescaled the velocity profiles with the velocity at r_i to highlight the qualitative changes. We have rescaled the radial coordinate with the average bubble radius $\langle d \rangle$, to hightlight the steep decay of the velocity profiles. We only plot a limited region of r since all velocity profiles are strongly shear banded. When we thus zoom in, we observe that nevertheless, the shape of the velocity profiles depends on the exerted rate of strain, as in the linearly sheared foam: the runs that were recorded at the highest driving velocity exhibit the most shearbanding. This is in strong contrast with the findings by Debrégeas et al. [9], were rate independent profiles were found. This is striking because we operate at essentially the same shear rates and because having only one bounding plate in stead of two, as for the Hele-Shaw cell employed in [9] should matter little as regards the bubble-wall drag force. We do observe approximately exponentially decaying profiles (see inset of Fig 3.3).

The shear banding cannot a priori be attributed to the bubble-wall

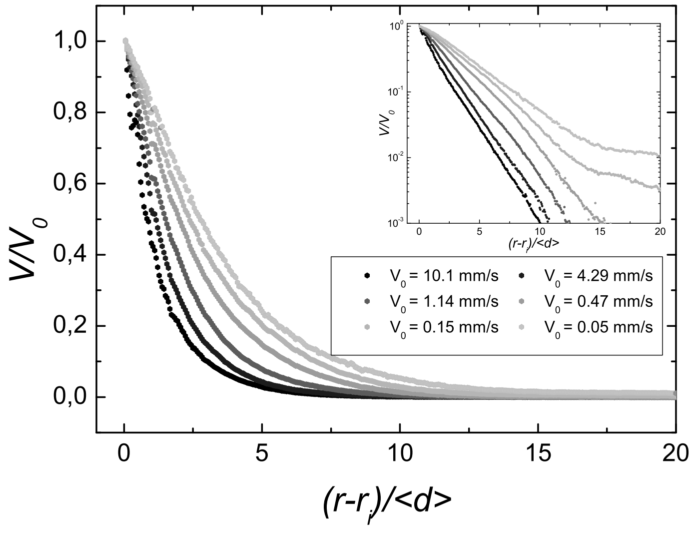

FIGURE 3.3: Velocity profiles for two dimensional Taylor-Couette flow of foam with top plate. We see strongly shear banded velocity profiles that furthermore exhibit rate dependence: the faster the driving velocity, the more shear banded the profiles become. Inset highlights approximately exponential decay of velocity profiles.

drag as another inhomogeneity in the stresses due to the curvature is present. However, by comparing to the results in the linear geometry we can venture a guess that in the Couette geometry the rate dependence is again due to the fact that the bubble-bubble drag and the bubble-wall drag scale with different exponents. By applying the drag force balance model to the cylindrical geometry, we will investigate this question in section 3.5.

To be able to perform bubble raft experiments, we place spacers between the supports and the glass plate. By doing so the bubbles are no longer confined. If we now lower the inner wheel, we can shear the foam without drag from the top plate. However, the foam stability is strongly decreased and bubbles will pop after approximately $1\frac{1}{2}$ hours. Nevertheless, the bubbles are sufficiently stable that we can shear the foam at the same shear rates as in the experiments with a bounding glass plate, except for the slowest run. Results are plotted in Fig. 3.4: within experimental

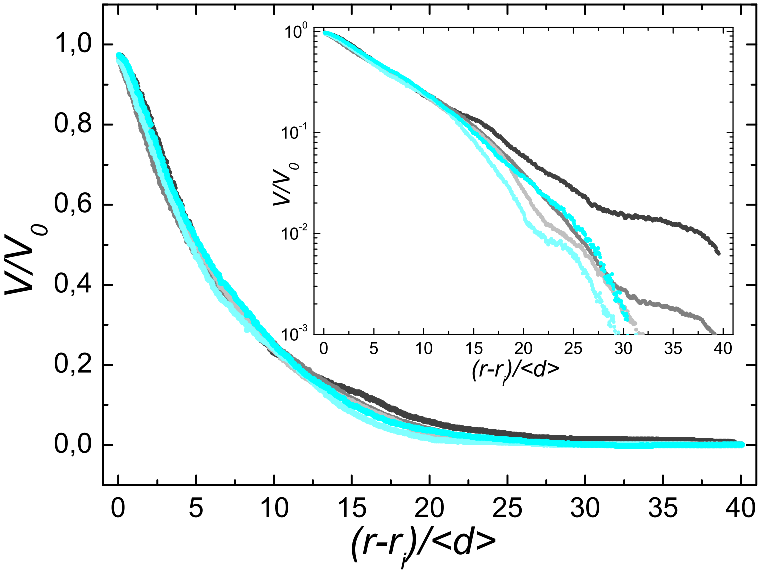

FIGURE 3.4: Velocity profiles for two dimensional Taylor-Couette flow of foam without top plate, the driving velocities are as in Fig. 3.3. We see approximately rate independent velocity profiles, with a curvature that is solely due to the curved geometry. We observe no discontinuous transition in the shear rate, as is evidenced by the log-lin inset, that furthermore highlights exponential decay near the inner disc.

uncertainty the profiles exhibit rate independent velocity profiles. We observe that the velocity profiles are still reasonably shear banded, but this curvature is due to the fact that the stresses decay as $1/r^2$ in the Couette geometry, as we will see later on. We furthermore observe no discontinuous transition between a flowing and a static region as was found by Rodts et al. [84] and Dennin and coworkers [68,71,87] experimentally and Cheddadi et al. theoretically [81].

3.4 Model

In this section we attempt to validate the drag force balance model developed for linear shear of two-dimensional foams by applying it to the circular case. We will proceed as follows: because the geometry has circu-

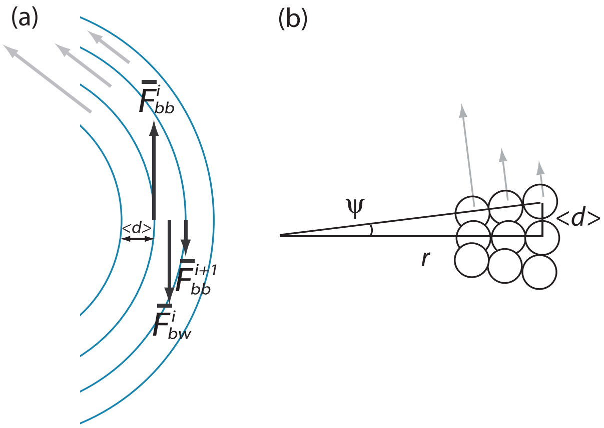

FIGURE 3.5: (a) Illustration of the model defined in Eq. (3.6): the light grey arrows indicate the velocity profile, while the black arrows indicate the resulting drag forces on lane i. (b) Schematic explanation of the additional term $v_i\langle d\rangle/r$ in Eqs. (3.3): bubbles in lane $i+1$ that have advanced by a distance $\langle d\rangle$ will exert a small inward drag force on bubbles in lane i of magnitude $[\sin\Psi \cdot v_i]^{\beta}$ with $\sin\Psi = \langle d\rangle/r$.

lar symmetry, this time instead of balancing drag forces on neighbouring lanes, we have to balance torques on neighbouring annuli, see Fig. 3.5. To arrive at the torques acting at lane i, we start with the expressions from Eq. (2.11) and adapt them to the circular geometry:

$$\overline{F}^{i}_{bw} = f_{bw}\left(\frac{\eta v_i}{\sigma}\right)^{2/3} , \tag{3.1}$$

$$\overline{F}^{i}_{bb} = f_Y + f_{bb}\left[\frac{\eta}{\sigma}(v_{i-1} - v_i - v_i\langle d\rangle/r)\right]^{\beta} , \tag{3.2}$$

$$\overline{F}^{i+1}_{bb} = f_Y + f_{bb}\left[\frac{\eta}{\sigma}(v_i - v_{i+1} - v_i\langle d\rangle/r)\right]^{\beta} . \tag{3.3}$$

In both bubble drag forces a new term $v_i\langle d\rangle/r$ has appeared, and we can explain these in two ways. Firstly, it turns out to be crucial to ensure that the continuum limit of the circular drag force balance model agrees with the Cauchy equilibrium criterion in polar coordinates, see Appendix 3A, that states that a body force acting in the azimuthal direction is balanced by:

$$\frac{\partial \tau}{\partial r} + \frac{2\tau}{r}, \tag{3.4}$$

with τ the stress. Furthermore, the strain rate in polar coordinates reads:

$$\dot{\gamma} = r\frac{d}{dr}\left[\frac{v_\theta(r)}{r}\right] = \frac{dv_\theta(r)}{dr} - \frac{v_\theta(r)}{r}. \tag{3.5}$$

From Eq. (3.5) we can thus already see the necessity of including a term $v_i\langle d\rangle/r$.

Secondly, we can construct a tentative picture of the origin of these forces in the spirit of our drag force balance model. This picture is illustrated in Fig. 3.5(b): due to the curvature, bubbles that have advanced in the θ-direction by a distance $\langle d\rangle$ in lane $i+1$ will exert a drag force in the inward radial direction, because these bubbles provide a steric hindrance for the bubbles in the i-th lane to move straight on. Similarly, bubbles that lag behind by a distance $\langle d\rangle$ will push the bubble in lane i outward. The radial component of the associated bubble velocity is given by $v\langle d\rangle/r$, thus giving rise to that additional term.

In the circular geometry we balance torques, and hence we balance the force per bubble times the number of bubbles $N^i \equiv 2\pi r/\langle d\rangle$ on rings of circumference $2\pi r$ and width $\langle d\rangle$, the average bubble diameter. The force balance then reads:

$$N^{i-1}2\pi(r - \langle d\rangle/2)\overline{F}^i_{bb} - N^i 2\pi r\overline{F}^i_{bw} - N^{i+1}2\pi(r + \langle d\rangle/2)\overline{F}^{i+1}_{bb} = 0. \tag{3.6}$$

The torque due to the bubble-bubble drag forces is evaluated a distance $\langle d\rangle/2$ from the center of bubble lane i. While this is indeed where this drag force acts, we did not need to specify this in the linear geometry. Again however, it turns out that specifying this distance is crucial to match the continuum limit to Eq. (3.4).

Since the resulting relative velocity vectors deviate by an angle $\Psi = \arcsin(\langle d\rangle/r)$ from the θ-direction, a factor $\sin(90\pm\psi) = \sqrt{1 - (\langle d\rangle/r)^2}$ $\approx 1 - \frac{1}{2}(\langle d\rangle/r)^2$ should be added in the viscous part of the bubble-bubble drags, but this is of higher order in $\langle d\rangle/r$ and we ignore it. The resulting expression can be written as:

$$
\begin{aligned}
(2\pi r)^2 f_{bw}\left[\frac{\eta v_i}{\sigma}\right]^{\frac{2}{3}} = {} & [2\pi(r-\frac{\langle d\rangle}{2})]^2\left(f_Y + f_{bb}\left[\frac{\eta}{\sigma}(v_{i-1} - v_i(1+\frac{\langle d\rangle}{r}))\right]^{\beta}\right) \\
& -[2\pi(r+\frac{\langle d\rangle}{2})]^2\left(f_Y + f_{bb}\left[\frac{\eta}{\sigma}(v_i(1-\frac{\langle d\rangle}{r}) - v_{i+1})\right]^{\beta}\right) \qquad (3.7)
\end{aligned}
$$

We can rewrite this as follows:

$$
\begin{aligned}
k(\frac{\eta v_i}{\sigma})^{2/3} = {} & \left(1-\frac{\langle d\rangle}{2r}\right)^2\left[\frac{\eta}{\sigma}(v_{i-1} - v_i(1+\frac{\langle d\rangle}{r}))\right]^{\beta} \\
- {} & \left(1+\frac{\langle d\rangle}{2r}\right)^2\left[\frac{\eta}{\sigma}(v_i(1-\frac{\langle d\rangle}{r}) - v_{i+1})\right]^{\beta} \\
- {} & \frac{2f_Y\langle d\rangle}{f_{bb}r}, \qquad (3.8)
\end{aligned}
$$

with $k = \frac{f_{bw}}{f_{bb}}$. We can take the units of length in which we measure - which is the average bubble diameter $\langle d\rangle$ and which we measure in units of the pixel length p - into account explicitly by making the substitution $f_{bb} \to f_{bb}^*$ with $f_{bb}^* = f_{bb}/(\langle d\rangle/p)^{1+\beta}$, which is the scale factor on the left hand side of Eq. (2.16).

3.4.1 Continuum limit

We have already stated that it is crucial to check if our numerical model is physically correct by comparing the continuum limit to Eq. (3.4). If we neglect quadratic terms in $\langle d\rangle/r$ we find from Eq. (3.7) (note that $\lim_{\langle d\rangle\downarrow 0}\langle d\rangle\frac{v_{i-1}-v_i}{\langle d\rangle} = -\frac{\partial v(r)}{\partial r}$):

$$
\begin{aligned}
k(\eta v_i/\sigma)^{2/3} = {} & \langle d\rangle\frac{\partial}{\partial r}\left(\frac{\eta\langle d\rangle}{\sigma}(\frac{\partial v(r)}{\partial r} - \frac{v}{r})\right)^{\beta} \\
& +\frac{2\langle d\rangle}{r}\left[\left\langle\left(\frac{\eta\langle d\rangle}{\sigma}(\frac{\partial v(r)}{\partial r} + \frac{v}{r})\right)^{\beta}\right\rangle + \frac{f_Y}{f_{bb}}\right]. \qquad (3.9)
\end{aligned}
$$

From Eq. (3.9), we can immediately deduce that the continuum limit of our model indeed satisfies both Eqs. (3.4) and (3.5) and that

$$
\tau = \left(\frac{\eta\langle d\rangle}{\sigma}\dot{\gamma}\right)^{\beta} + \frac{f_Y}{f_{bb}}. \qquad (3.10)
$$

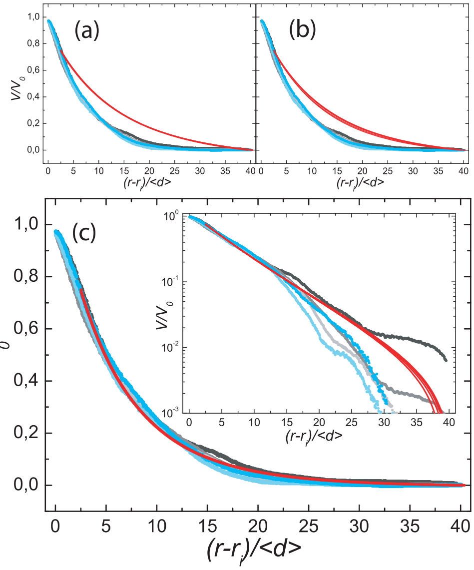

FIGURE 3.6: (a)+(b)+(c): Data from Fig. 3.3. (a)+(b): Solid lines are solutions to the drag force balance model defined in Eq. (3.8), with k =0 since top plate drag is absent, β =0.36 and $f_Y = 0$ (a) or $f_Y = 1.2 \times 10^{-5}$ N (b). Clearly, for $\beta = 0.36$ the fits are far off (a), whereas setting f_Y to the value found in Fig. 2.12(b) results in a small rate dependence which is in fact more pronounced for fits with $\beta = 0.20$. (c) Solid lines are model profiles with $\beta = 0.20$ and $f_Y = 0$. Inset shows data on a lin-log scale: both the model and the experimental profiles curve downwards, since they have to obey $v(r_o) = 0$.

Eq. (3.5) shows the necessity of introducing the terms $v_i d/r$ in the drag forces $\overline{F}_{bb}$: it accounts for the curvature term in the ensuing continuum version of the model.

3.5 Fits

3.5.1 Flows without a top plate

We match solutions of our curved drag force balance model Eq. (3.8) to the experimental velocity profiles in the following way. For the case without a top plate, $f_{bw} = 0$ and hence the constant $k = 0$. Thus our model simplifies, and only contains two fit parameters: the exponent β, and the yield force f_Y. Surprisingly, when we take for beta the value obtained from the linear geometry and rheology, $\beta = 0.36$, we have not been able to obtain a convincing fit, see Fig. 3.6(a). Moreover, using in addition the estimate of f_Y from rheology, see Fig. 2.12(b), makes the fits even worse, see Fig. 3.6(b), as it introduces a small rate dependence. However, a good fit to the model can be obtained by taking $\beta = 0.20 \pm 0.02$ and f_Y at least one order of magnitude smaller than the value from Fig. 2.12(b) $\rightarrow f_Y \leq 1.2 \times 10^{-6}$. The yield drag then essentially has no influence on the shape of the model fits and we could as well set it zero.

We show the data, fit to solutions of the model with $\beta = 0.20$, $k = 0$ and $f_Y = 1.2 \times 10^{-6}$ N in Fig. 3.6: the model solutions fit reasonably well to the data and correctly capture the rate-independence for the bubble raft experiment.

3.5.2 Flows with a top plate

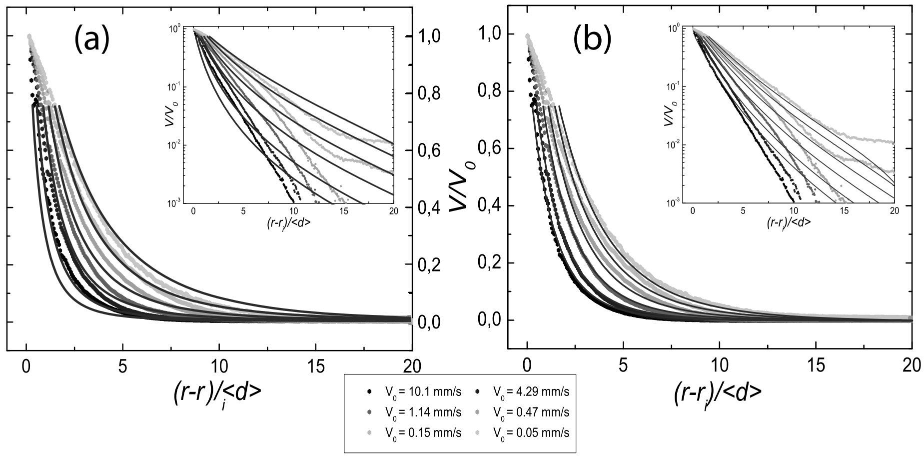

FIGURE 3.7: (a) Same data as in Fig. 3.4. Solid lines are solutions to the drag force balance model defined in Eq. (3.8), with k =15.5 β =0.20 and $f_Y = 0$ N. (b) Again data from Fig. 3.4. Solid lines are solutions to the drag force balance model, with k =5.5 β =0.36 and $f_Y = 0$ N. The quality of the fit is markedly improved.

For the case with a top plate, we have in principle three fit parameters.

To extract the optimal value of β we look for a minimum in the spread of k over all six runs while setting $f_Y = 0$ — setting $f_Y = 1.2 \times 10^{-5}$ yields poor fits. For every $0.30 < \beta < 0.60$ there seems to a rather good fit to all the profiles if k is tuned properly, and only at $\beta < 0.30$ the spread in k-values increases significantly. For $\beta = 0.20$ the model profiles fit downright poorly, Fig. 3.7. We also show fits to the data with k =5.5 and β =0.36 to highlight the fact that we can reproduce the correct trend in rate dependence and obtain rather good fits in the range $0.30 < \beta < 0.60$.

3.6 Local rheology and power-law fluids

As discussed above, the value of the yield drag force f_Y we extracted from our fits is anomalously small compared to the value found from bulk rheometry. This could be either due to the yield stress being much lower locally than what is measured in bulk rheometry [88], consistent with the idea of a static and dynamic yield stress. Another option is that a local stress strain relation is not satisfied throughout the gap, placing severe restrictions on the validity of comparing the experimental velocity profiles with the model profiles. Finally, the yield stress could simply not play a role in these foam flows. Another issue is the conflicting value of the β extracted from our fits and β as established in chapter 2: the bubble raft experimental profiles are best fit with a $\beta = 0.20 \pm 0.02$ which is much lower than $\beta = 0.36$ found in chapter 2.

We will investigate these issues in two ways. The first is by fitting the velocity profiles obtained in the freely flowing bubble raft to the analytical prediction for velocity profiles of power law fluids (hence without a yield stress) in a Couette geometry, to see if a yield stress is needed to fit the velocity profiles. We will then present additional measurements obtained by simultaneously imaging the velocity profiles and measuring the bulk rheometrical response of a two dimensional bubble raft in a Taylor-Couette geometry. This allows us to investigate the local rheology of the foam in the spirit of [79] and connect bulk rheometry with local measurements as well as our model solutions.

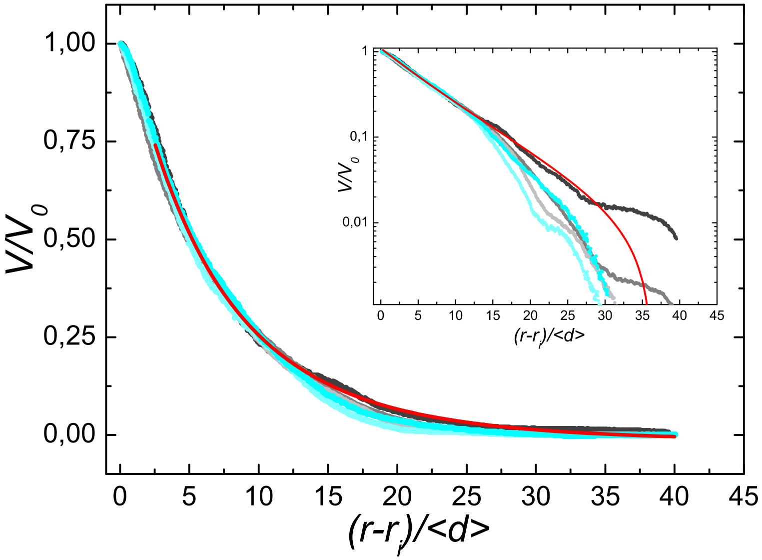

FIGURE 3.8: Velocity profiles for foam without top plate with analytical solution to Eq. (3.11). Note the reasonable agreement, even though this model does not consider a yield stress.

3.6.1 Fit to a power-law fluid model

If the yield stress is assumed to be absent, one can analytically solve the following equation for the stresses in the system:

$$\tau(r) = \frac{T}{r_i r^2} = k \left(\frac{\eta \langle d \rangle}{\sigma} \right)^{\beta} \dot{\gamma}^{\beta} \equiv C \left(r \frac{d}{dr} \frac{v_\theta(r)}{r} \right)^{\beta}. \tag{3.11}$$

The solution to this differential equation is given in Appendix B. We can vary β and obtain an optimal match with the experimental velocity profiles obtained in the shear cell without top plate for $\beta = 0.20$. The analytical velocity profile adequately fits the data and the value of β is in good agreement with the exponent found previously by fitting the model profiles to the experimental data. This strongly indicates that the yield stress has a negligibly low influence on the shape of the velocity profiles and that we can essentially understand the shape of the experimental velocity profiles to stem from the power-law fluid nature of the two dimensional foam, without accounting for the yield stress. The question remains, however, *why* we do no observe a yield stress and *what* sets the anomalously low exponent.

3.6.2 Rheometry: an anomalous local flow rule

We can try to see if a local flow rule describes the foam rheology throughout the system, as this would validate fitting a local drag force balance model to the experimental profiles as well as show possible non-local effects that might influence the flow in this system. To this end, we shear a bidisperse monolayer of foam bubbles in an Anton Paar DSR 301 rheometer. We again employ a Taylor-Couette geometry, but this time we can measure torques on the inner cylinder which is connected to the rheometer head (lower inset of Fig. 3.9). We impose five different strain rates, spanning two decades in total and measure the resulting average torque, while simultaneously imaging the bubble motion from which we can calculate the averaged velocity profiles. The radii of the inner disc and the outer ring are $r_i = 0.025$ m and $r_o = 0.07$ m. The resulting velocity profiles are displayed in Fig. 3.9: within experimental uncertainty the profiles are rate independent, as well as strongly localized. Again we observe no discontinuity in the local strain rate.

We fit solutions of the drag force balance model to the velocity profiles and we obtain optimal fits for $\beta = 0.20 \pm 0.02$ and $f_Y = 0$ (red curves in Fig. 3.9). Clearly, these fits do not extend over the whole velocity profile and we will shortly see this is due to the absence of a local flow rule near the inner disc.

We will now calculate local stresses and strain rates throughout the gap of our Couette cell, with a method that was utilised in [79, 85, 89]. From the Cauchy equilibrium condition we know that the stresses in the system are given by (see Appendix 3.A for details):

$$\tau(r) = \tau(r_i) r_i^2 / r^2. \tag{3.12}$$

Furthermore, we can take the appropriate derivative, Eq. (3.5), of the velocity profile:

$$\dot{\gamma} = r \frac{d}{dr} \left[\frac{v_\theta(r)}{r} \right] \tag{3.13}$$

to obtain the local strain rate $\dot{\gamma}(r)$. We then have for each r-coordinate a value of the local stress and the local strain rate and we can thus plot

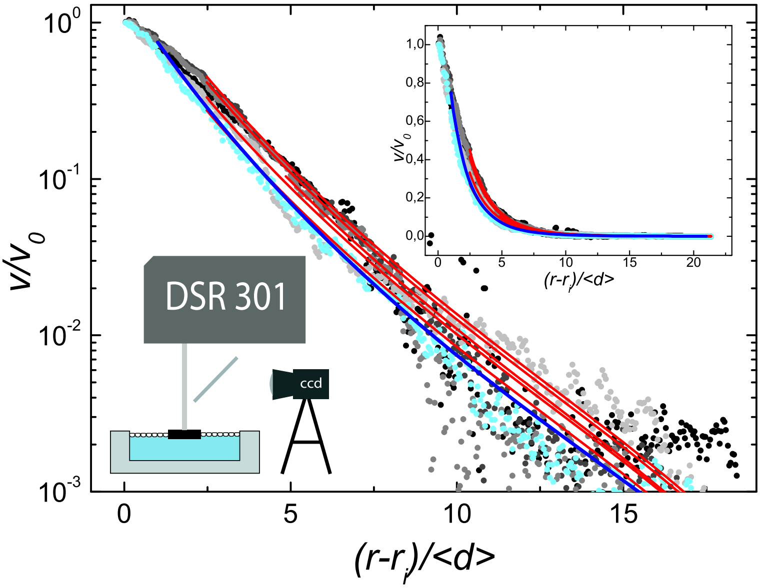

FIGURE 3.9: Averaged velocity profiles plotted on log-lin scale from a bubble raft sheared in Taylor-Couette geometry with inner disc driven by rheometer head. Solid lines: fits to drag force balance model with $\beta = 0.20 \pm 0.02$ and $f_Y = 0$. Upper inset shows same plot on linear scale to highlight the part of the profile where one can fit. Blue curve: Velocity profile for power-law fluid (analytical solution Eq. (3.11)) with $\beta = 0.22$. Lower inset: schematic picture of the setup.

the local stress as a function of the local strain rate, which is displayed in Fig. 3.10. The local rheology of the experimental velocity profiles is given by the five scatter plots ranging from black to light blue.

If there truly were a local flow rule then al these profiles would collapse onto one master curve. However, we can clearly see from Fig. 3.10 that all profiles start to deviate from the flow curve at a point — labeled by a yellow square in Fig. 3.10 — close to the inner cylinder, where the local stresses are high.

A direct consequence is that fitting the velocity profiles with our local drag force balance model at a radial distance that is closer to the inner cylinder than this divergence point is useless. If we, however, restrict ourselves to the parts of the velocity profiles where the local flow rule is obeyed we can excellently fit our experimental data (see Fig. 3.9).

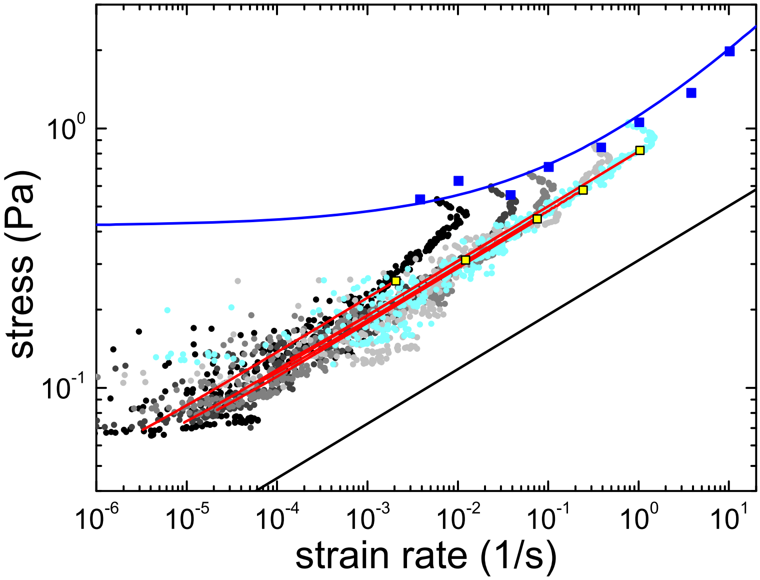

FIGURE 3.10: (b) Local stress-strain relation extracted from velocity profiles in Fig. 3.9: The local strain rate can be calculated from the velocity profiles and the stress is known from the measured torque. Scattered data: local stress-strain relation for experimental profiles. Red solid lines: Model profiles from Fig. 3.9. Yellow squares: maximal value of the local rate at which a local flow rule — and hence the fit — holds. Blue dots: bulk rheometrical measurements. Solid blue line: Herschel-Bulkley fit through bulk data points: $0.42 + 0.7\dot{\gamma}^{0.36}$. Black line: power law with slope 0.21.

The red lines in Fig. 3.10 denote the local stress- strain rate behaviour of the model profiles and not surprisingly, since these profiles are essentially solutions to a power-law constitutive equation (Eq. (3.9), with $f_Y = 0$) they nicely collapse and scale as $\dot{\gamma}_l^{0.21}$ as shown by the solid black line.

The blue squares denote the measured torque at the inner disc for the corresponding velocity profiles plus two additional data points at high shear rate to facilitate fitting a Herschel-Bulkley expression (solid blue line). We cannot image at sufficiently high frame rates to record the flow at these high shear rates and thus we have no information on the local rheology there.

3.7 Discussion

Three things strike the eye in Fig. 3.10: *i)* Both experimental profiles and the model solutions exhibit a local flow rule that reads $\tau \propto \dot{\gamma}^{0.21}$, in clear contradiction with the previously found exponent $\beta = 0.36$. Nevertheless, this value 0.21 is in good agreement with the exponent extracted from fitting an analytical power-law fluid model to the experimental velocity profile. It is also consistent with the optimal fits of the model profiles in both Fig. 3.6(c) and Fig. 3.9.

ii) By plotting the bulk stress and strain rate as measured by rheometry and the corresponding Herschel-Bulkley fit we see that, in the tails of the velocity profile, the foam still flows well below the global yield stress. This confirms the finding that the optimal fits from the drag force balance model were obtained at f_Y at least one order of magnitude lower than the value as found in bulk rheometry: the global extrapolated yield stress in Fig. 3.10 is far above the local stresses, in fact we do not observe a yield plateau for our range of local strain rates.

iii) Due to the large stress and strain rate gradients near the inner disc, one apparently only measures the non-local flow behaviour with the rheometer and one can thus measure a different rheology with the rheometer — $\tau = \tau_Y + k\dot{\gamma}^{0.36}$ — than what actually governs the local flow, which reads $\tau = k\dot{\gamma}^{0.21}$. This finding is in clear contrast with [85] where, for wide-gap Couette rheometers the local and global flow behaviour obey exactly the same constitutive equation. However, the large local strain rates near the inner disc in our experiment might give rise to a non-local rheology in the spirit of Goyon et al. [79], where rearrangements in the shearing zone lead to cooperative flows in the shear bands.

Since measuring an exponent $\beta = 0.36$ seems to be a result of non-typical rheology close to the inner disc, it is an open question why a local strain rate scaling with $\beta = 0.36$ describes *linear* shear flow of two-dimensional foams bounded by a glass plate so well. We hypothesise it might have to do with the type of flow in the foam: optical inspection of foam regions where the local strain rate is very low, evidence qualitatively different behaviour between the bubble raft flow and the liquid-glass flow. A qualitative difference in the fluctuations might well be at the root of this behaviour, and we will present a simple optical technique that seems to support this explanation in chapter 5. This would also explain the poor fit with $\beta = 0.20$ of the rate dependent runs in Fig. 3.6(b).

3.8 Conclusion

We have measured velocity profiles in a two-dimensional foam monolayer, undergoing cylindrical (Taylor-Couette) shear. We have adapted our drag force balance model to the circular geometry and have obtained model fits that adequately fit the experimental data for the foam without a top plate, with a bubble-bubble drag force exponent $\beta = 0.20$, much smaller than was measured in the linear geometry. Also, the yield stress required to obtain good fits is either zero or at least one order of magnitude smaller than the value previously obtained from two-dimensional rheometry. In order to elucidate the role of the yield stress and non-locality on our foam flow we have performed additional rheometry and velocimetry on foams in a smaller Taylor-Couette geometry. From these measurements we can extract the local stress-strain rate relation throughout our sample and we observe a local flow rule $\tau \propto \dot{\gamma}^{0.20\pm0.02}$, from which deviations occur close to the inner cylinder that place a bound on the range of the velocity profiles to which we can fit our model. Furthermore, the foam appears to flow at stresses well below the yield stress.

Fitting the analytical expression for velocity profiles for power-law fluids (hence without a yield stress) to the experimental profiles yields a power-law index 0.21, in good agreement with the directly measured local stress-strain rate relation.

Appendices

3.A Stress and strain rate in polar coordinates

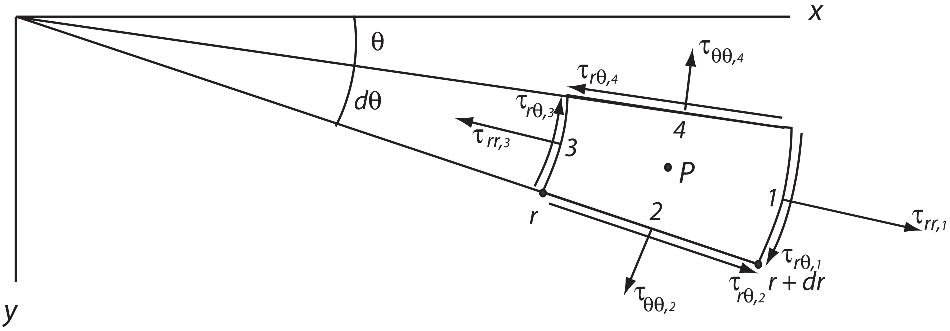

FIGURE 3.11: Infinitesimal element used to derive Cauchy equilibrium in polar coordinates.

A consideration of the stresses and strains in the Couette experiment is best performed in polar coordinates (r, θ), which are related to Cartesian coordinates through

$$r = \sqrt{x^2 + y^2} \quad , \quad \theta = \arctan(y/x), \tag{3.14}$$

$$x = r\cos(\theta) \quad , \quad y = r\sin(\theta) \tag{3.15}$$

3.A.1 Stress equilibrium

We will here follow the excellent geometrical derivation of the Cauchy equilibrium condition for the stresses and strain(rate) in polar coordinates found in [90]. Consider a infinitesimally small element with vertices located at (r, θ), $(r, \theta + d\theta)$, $(r + dr, \theta + d\theta)$ and $(r + dr, \theta)$ (see Fig. 3.11). We can then find the Cauchy equilibrium conditions by looking at the radial and the tangential force balance at P separately.

The radial force on side 1 is $\tau_{rr,1}(r + dr)d\theta$ and similarly the radial force on side 3 is $-\tau_{rr,3}rd\theta$. The normal force on side 2 has a component along the radial direction of $-\tau_{\theta\theta,2}dr\sin(d\theta/2) \simeq -\tau_{\theta\theta,2}drd\theta/2$ as does the normal force on side 4: $-\tau_{\theta\theta,4}drd\theta/2$. The shear stresses result in a force

$(\tau_{r\theta,2} - \tau_{r\theta,4})dr$. If we sum up these forces and include a body force R we obtain the equation of equilibrium in the radial direction:

$$\begin{aligned}\tau_{rr,1}(r+dr)d\theta - \tau_{rr,3}rd\theta \quad &- \quad \tau_{\theta\theta,2}drd\theta/2 - \tau_{\theta\theta,4}drd\theta/2 \\ &+ \quad (\tau_{r\theta,2} - \tau_{r\theta,4})dr + Rrd\theta dr = 0. \end{aligned} \quad (3.16)$$

If we divide this by $drd\theta$ we find:

$$\frac{\tau_{rr,1}(r+dr) - \tau_{rr,3}r}{dr} - \frac{\tau_{\theta\theta,2} + \tau_{\theta\theta,4}}{2} + \frac{\tau_{r\theta,2} - \tau_{r\theta,4}}{d\theta} + Rr = 0. \quad (3.17)$$

By taking the limit $dr, d\theta \downarrow 0$ we find the equilibrium condition for the radial stresses:

$$\frac{\partial(r\tau_{rr})}{\partial r} + \tau_{\theta\theta} + \frac{\partial \tau_{r\theta}}{\partial \theta} + rR = 0. \quad (3.18)$$

Dividing by r yields the normally encountered expression:

$$\frac{\partial \tau_{rr}}{\partial r} + \frac{1}{r}\frac{\partial \tau_{r\theta}}{\partial \theta} + \frac{\tau_{rr} - \tau_{\theta\theta}}{r} + R = 0. \quad (3.19)$$

For the tangential stress balance we can perform the exact same analysis and we find the balance to read:

$$(\tau_{\theta\theta,2} - \tau_{\theta\theta,4})dr + (\tau_{r\theta,4} - \tau_{r\theta,2})drd\theta + (\tau_{r\theta,1}(r+dr) - \tau_{r\theta,1}r)d\theta = 0. \quad (3.20)$$

By taking the limit $dr, d\theta \downarrow 0$ we find the tangential stress balance, which reads:

$$\frac{1}{r}\frac{\partial \tau_{\theta\theta}}{\partial \theta} + \frac{\partial \tau_{r\theta}}{\partial r} + 2\frac{\tau_{r\theta}}{r} = 0. \quad (3.21)$$

3.A.2 Strain and strain rate

While the expression for the strain rate can be obtained by straightforward coordinate substitution [91], one can again consider an infinitesimal element that is deformed by an amount w in the radial direction and u in the tangential direction. A detailed derivation is given in [90]. We will restrict ourselves to stating the results. The shear strain $\gamma_{r\theta}$ is given by:

$$\gamma_{r\theta} = \frac{\partial w}{r\partial \theta} + \frac{\partial u}{\partial r} - \frac{u}{r}. \quad (3.22)$$

Due to the rotational symmetry, the first term is 0. If we take the time-derivative we find the shear strain rate:

$$\dot{\gamma}_{r\theta} = \frac{\partial v}{\partial r} - \frac{v}{r} = r\frac{\partial}{\partial r}\left[\frac{v}{r}\right]. \quad (3.23)$$

3.B Velocity profiles for a power-law or a Herschel-Bulkley fluid in a curvilinear geometry

In a Taylor-Couette Geometry with inner and outer radii r_i and r_o, Eq. (3.21) dictates the balance of stresses in the tangential direction. Since the flow has rotational symmetry, all the terms in Eq. (3.19) equal 0 and in the tangential stress balance, $\frac{1}{r}\frac{\partial \tau_{\theta\theta}}{\partial \theta} = 0$. Eq. (3.21) then reads:

$$\frac{\partial \tau_{r\theta}}{\partial r} + 2\frac{\tau_{r\theta}}{r} = 0. \tag{3.24}$$

The solution to this differential equation is given by

$$\tau(r) = \tau(r_i) r_i^2 / r^2. \tag{3.25}$$

For a power-law fluid, the stresses are balanced by the local strain rate [68]:

$$\tau(r) = \frac{\tau(r_i) r_i^2}{r^2} = k\dot{\gamma}^{\beta} = k\left[r\frac{\partial}{\partial r}\left(\frac{v}{r}\right)\right]^{\beta}. \tag{3.26}$$

This simplifies to:

$$\frac{(\tau(r_i) r_i^2)^{1/\beta}}{r^{2/\beta+1}} = \frac{\partial}{\partial r}\left[\frac{v}{r}\right]. \tag{3.27}$$

Which can be directly integrated, yielding:

$$\frac{v(r)}{r} = \frac{\beta}{-2}\frac{(\tau(r_i) r_i^2)^{1/\beta}}{r^{2/\beta}} + C \tag{3.28}$$

The integration constant C can be evaluated by requiring that $v(r)/r = 0$ at $r = r_0$. Thus we end up with:

$$v(r) = \frac{\beta}{2}(\tau(r_i) r_i^2)^{1/\beta} r \left[\frac{1}{r_o^{2/\beta}} - \frac{1}{r^{2/\beta}}\right] \tag{3.29}$$

We can of course add a yield stress term to the right hand side of Eq. (3.26), to model a Herschel-Bulkley fluid. However, an analytical solution is then no longer available, and one then needs to resort to numerical integration.